ISSN 1547-4771, Physics of Particles and Nuclei Letters, 2019, Vol. 16, No. 1, pp. 6–15. © Pleiades Publishing, Ltd., 2019.

METHODS OF PHYSICAL EXPERIMENT

Towards a Realistic Monte Carlo Simulation of the MPD Detector at NICA[1]

V. Kolesnikov[a], A. Mudrokh[a], V. Vasendina[a], and A. Zinchenko[a, *]

[a] *Joint Institute for Nuclear Research, Dubna, Moscow oblast, 141980 Russia*

**e-mail: Alexander.Zinchenko@jinr.ru*

Received August 17, 2018

Abstract—During the preparation of the physics program of any experiment it is very important to perform a realistic simulation of the detector, i.e. to describe real detector effects with as many details as possible. In this paper the current status of such a simulation of the MPD TPC (Time Projection Chamber) is demonstrated, including description of relevant processes. Data reconstruction approaches are also presented along with the main results on detector performance.

DOI: 10.1134/S1547477119010084

1. INTRODUCTION

The NICA heavy-ion program is aimed at the experimental investigation of the nuclear matter properties under extreme conditions [1]. It implies a detailed energy and system size scan with beam species varying from protons to gold nuclei in the center-of-mass energy range from 4 to 11 GeV per nucleon. The NICA physics program addresses variety of the fundamental phenomena in the strongly interacting matter: reaction dynamics, nuclear matter Equation Of State (EOS), nature of the deconfinement phase transition, in-medium modification of hadron properties, critical phenomena, and hypernuclei production. The emphasis will be put on the study of the yields, transverse momentum spectra, rapidity distributions, azimuthal anisotropy, event-by-event fluctuations and correlations of multiple probes from electrons and gammas to light (hyper)nuclei.

Most of the observables require a large phase-space coverage. For example, in the search for the QCD Critical End Point (CEP) by means of baryon number fluctuations, the number of identified in an event protons is a crucial parameter of the study. By increasing the particle identification (PID) coverage of the experimental setup from the midrapidity region (typically localized within the pseudorapidity window $|\eta| < 1$) up to $|\eta| < 2$ allows one to get a roughly 50% gain in the proton per-event statistics. Moreover, in contrast to very high collision energies the fireball properties at NICA vary over the reaction phase-space, thus, in order to map accurately the QCD phase diagram in terms of its thermodynamical parameters μ_B (baryochemical potential) and T (temperature) one needs to measure particle production practically up to the fragmentation region.

In order to fulfill the NICA physics program goals the MPD detector is designed as a large acceptance spectrometer providing high-efficiency tracking performance, precise vertex reconstruction (including the primary and secondary vertices), powerful particle identification (PID), as well as careful determination of the event centrality and event plane [2].

However, until now almost all the MPD feasibility study results on the strangeness [3], dileptons [4], and hypernuclei [5] have been obtained for the midrapidity region ($|\eta| \lesssim 1.2$). The TPC response model for these studies was based on a simplified approach to the hit production algorithm: a so-called "Gaussian smearing" was used, i.e. each detector hit produced by the Geant transport program was randomly displaced in longitudinal and transverse directions according to the space resolution parameters measured for similar detectors (normal distributions of $\sigma_t = 0.5$ mm and $\sigma_l = 1.0$ mm for the transverse and longitudinal directions, respectively).

In order to get more realistic estimates of the MPD performance, especially at forward pseudorapidities, a new approach that includes full simulations of the detector response is needed. This is the ultimate goal of our current activity. In this paper we present the first results of the TPC tracking performance study based on the realistic detector response simulation and respectively tuned cluster, hit and track finding procedures. The material is structured as follows. In the next chapter, the details of simulation of physics processes relevant for cluster formation inside the TPC volume are presented. Then, the procedures of the hit and

[1] The article is published in the original.

Table 1. TPC parameters used in this study

Parameter	Value
Magnetic field	0.5 T
Drift gas	P10 (90% Argon + 10% Methane)
Drift velocity	5.45 cm/μs
Transverse diffusion (σ_T) at 0.5 T	185 μm/$\sqrt{\text{cm}}$
Longitudinal diffusion (σ_L)	320 μm/$\sqrt{\text{cm}}$
Pad size	5×12 mm^2 (27 rows) + 5×18 mm^2 (26 rows)
Electronics shaping time (FWHM)	180 ns
ADC dynamic range	12 bits
ADC sampling frequency	10 MHz

track reconstruction are described. In the following, the TPC simulation results in terms of space and double-hit resolution as well as tracking efficiency and momentum resolution are presented. Finally, preliminary results on hyperon reconstruction are shown and a planning of future activities is given.

2. TPC SIMULATION

A data processing model during the MPD TPC simulation consists of the following steps:

(1) Event generation;

(2) Particle transport;

(3) TPC response simulation;

(4) Cluster/hit finding;

(5) Track reconstruction including energy loss dE/dx determination;

(6) Physics analysis: PID, secondary vertex finder, etc.

In this study we use the UrQMD [6] and DCM-QGSM [7–9] event generators as an input for simulation (item 1 above). The transport of particles through the detector is handled by the Geant3 package (item 2). The third item is based on the *microsimulation* procedure which internally uses TPC parameters listed in Table 1.

In the *microsimulation* procedure, the following processes are considered:

- primary ionization simulation (ionization clusters);
- drift and diffusion of ionization electrons;
- gas gain fluctuations according to the Polya distribution;
- charge distribution on the readout pad plane—pad response;
- electronics shaping;
- signal digitization in the ADC.

The ionization losses simulated by Geant in the TPC volume along the trajectory of a charged track are converted into the number of electrons which are then transported in the uniform electric field toward the anode wires. Both transverse and longitudinal diffusion are considered during the transport process of the electron cloud. The charge collected on the sense wire plane is affected by the electron gas multiplication process described by the Polya distribution. The final charge is distributed over readout pads in accordance to the pad response function determined from a study of the TPC prototype. The response of the readout electronics (i.e. shaping preamplifier with a 180 ns FWHM shaping time) is folded with the electron drift time distribution. Finally, all the pad signals are digitized in ADCs with a 12-bit precision. A threshold of 10 ADC counts is applied which is equivalent to the expected level of the noise in the TPC readout channel—zero suppression procedure.

Some examples of the charge distributions obtained after the zero suppression procedure can be seen in Fig. 1 (top row). Shown are the ADC count distributions versus pad and time bucket numbers for the case of a three-track cluster. As can be seen, the originally generated space point positions (their coordinates are shown on the left panel by white circles) closely match those of the simulated and reconstructed clusters (squares).

3. CLUSTER/HIT RECONSTRUCTION IN TPC

To check the TPC performance (Sections 3–5) we use the UrQMD generated event sample of central Au + Au collisions at $\sqrt{s_{NN}} = 9$ GeV.

The original cluster/hit finding procedure included the following main steps:

- finding preclusters (groups of adjacent pixels in time bin—pad space after zero suppression);
- finding separated local maxima in the preclusters using the "peak-and-valley" approach;
- reconstruction of the coordinates of the found local maxima via center-of-gravities.

The "peak-and-valley" approach consists in finding local maxima ("peaks") in the charge vs. time bin

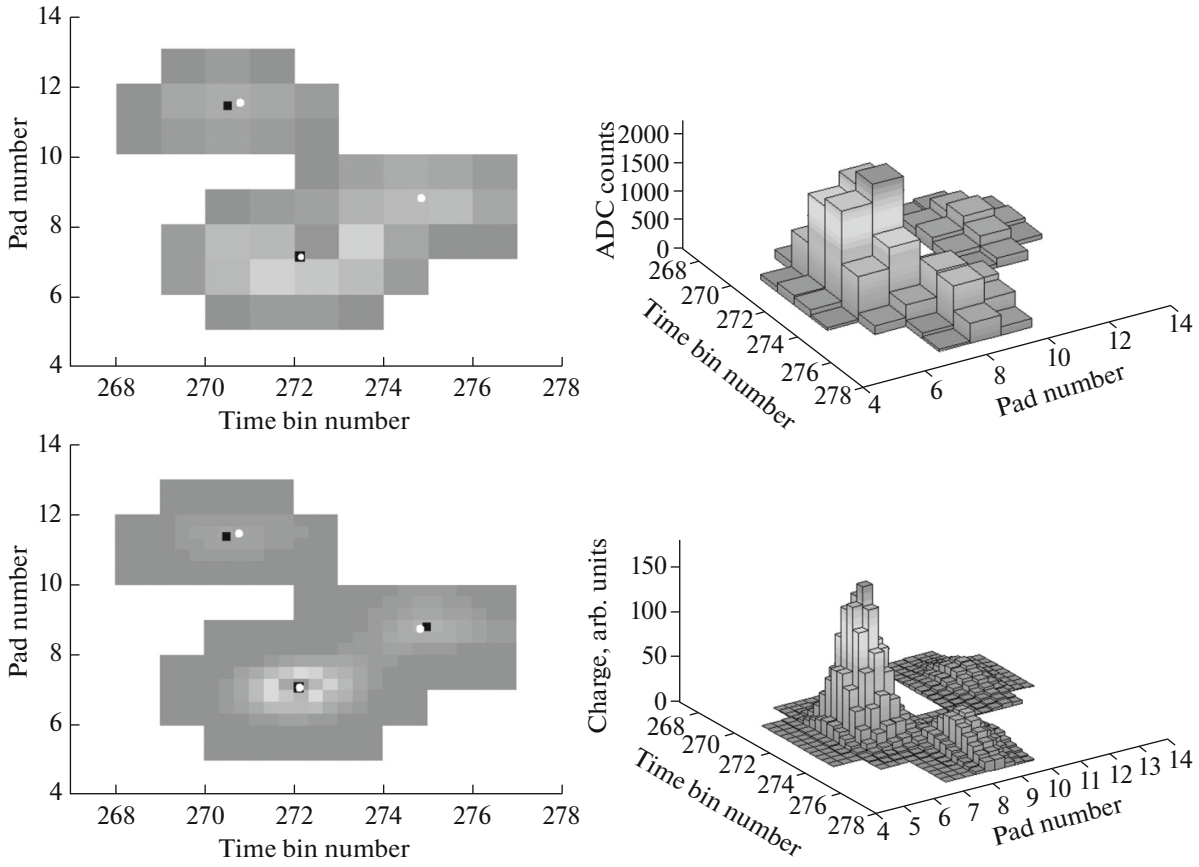

Fig. 1. Top—2D and 3D views of a precluster of three tracks. The true hit coordinates are indicated by circles, the reconstructed ones are shown by squares. On the top left plot one hit has not been reconstructed. Bottom—2D and 3D views of the same precluster after the MLEM procedure (see text for details).

vs. pad number domain separated by sufficiently deep "valleys". The granularity of the time bin—pad number plane (let us call it a pad space) is defined by the readout pad transverse size (5 mm) and the ADC sampling frequency (~5.45 mm). It was found that for a non-negligible fraction of preclusters produced by several close-by tracks the "peak-and-valley" criterion failed to separate local maxima due to insufficient granularity of the pad space (see the top row of Fig. 1). To cope with this, a more sophisticated cluster finding algorithm, based on the charge distribution deconvolution, was developed.

The new approach exploits a so-called Maximum Likelihood—Expectation Maximization (MLEM or EM) deconvolution technique [10] (also known as Lucy–Richardson method [11, 12] or Bayesian unfolding [13]). The essence of the method is that it iteratively solves the inverse problem of a distribution deconvolution. It was widely used in nuclear medicine for tomographic image reconstruction, and was also succesfully tried for hit finding in silicon drift detectors [14] and cathode pad chambers [15].

The MLEM procedure starts from creating a set of pixels with sizes equal to 1/3 of the original pads. It is assumed that each pixel contains a track. If the initial value of a charge release from a track j (i.e. pixel intensity) was p_j^0 (usually all p_j^0's are set to 1) then the following iterative procedure will update its value:

$$p_j^{k+1} = \frac{p_j^k}{\sum_{i=1}^{N_{\text{pads}}} c_{ij}} \sum_{i=1}^{N_{\text{pads}}} c_{ij} \frac{q_i}{f_i^k} \quad \text{with} \quad f_i^k = \sum_{j=1}^{N_{\text{pix}}} c_{ij} p_j^k, \qquad (1)$$

where f_i^k is the expected signal on pad i if the pixel intensity was p_j^k (at the kth iteration), c_{ij} is the pixel-to-pad coupling (also known as the point spread function (PSF) or convolution kernel) and N_{pix} is the number of pixels in the array. The point spread function is a known characteristic of any detector, i.e. its response to a single track. However, in case of the TPC, PSF depends on the track direction. Fortunately, track direction can be evaluated with adequate accuracy from the precluster longitudinal position estimate.

After several iterations (5–10) the procedure stops and the "peak-and-valey" search is performed in the pixel space. As can be seen from the bottom row of

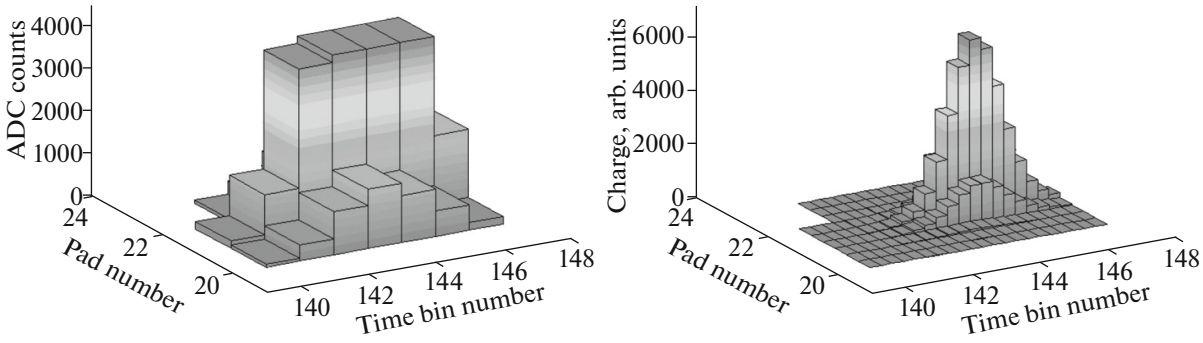

Fig. 2. 3D view of a cluster with overflows. Left—ADC output, right—after MLEM procedure.

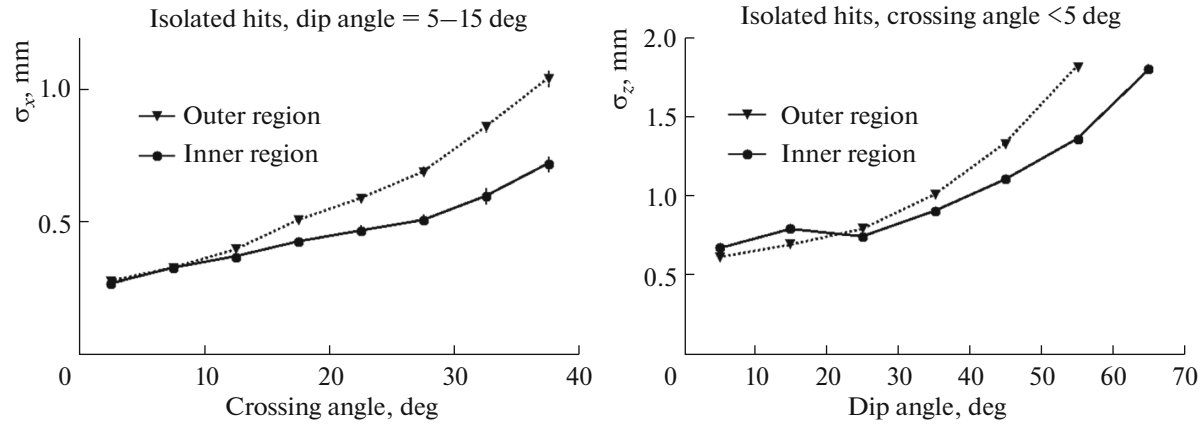

Fig. 3. Left—position resolution along the pad rows for tracks with the dip angle range 5–15 deg; right—position resolution along the z-axis of the TPC for tracks with the crossing angle below 5 deg. The crossing angle is the angle between the particle momentum and the pad row direction. The dip angle is the angle between the particle momentum and the normal to the drift direction. The results were obtained for isolated hits, i.e. for those not having a neighbor closer than 5 cm in any direction.

Fig. 2, the MLEM approach effectively improves the granularity of the detector. Moreover, the method allows one to partially recover from some information loss, i.e. for clusters with ADC overflows (digitized signal exceeding the dynamic range of ADC) it is possible to reconstruct the original charge distribution using pads with undistorted signals (Fig. 2). Since the number of pixels is 9 times larger than the number of original pads and the procedure requires several iterations, it is applied only for complex cluster topologies to speed up the processing, i.e. only for preclusters with more than 1 local maximum in the pad space or with overflows.

The results on the TPC coordinate reconstruction accuracy are shown in Fig. 3 where the resolutions along the pad row (transverse direction) and z-axis (drift direction) are plotted as functions of the pad row crossing angle and dip angle, respectively. As can be seen, at non-zero crossing (dip) angle the spatial resolution along x (z) degrades faster in the outer part of the TPC where the pad height is larger. The position resolution along the pad row (r–ϕ direction) is about 250 μm that is in agreement with the results obtained for the TPCs of a similar design (TPC of the STAR experiment, for example [16]).

Figure 4 demonstrates 2-hit separation capability of the MPD TPC. The efficiency of finding two hits as a function of the distance between them is consistent with a simple expectation that a (3–4) × w_{pad} separation is needed in order to be resolved (w_{pad} is the pad width). The efficiency weakly depends on whether hit is registered in the inner or outer part of the TPC. In the drift direction two hits are fully resolved if they are separated by more than 3 cm. One can see also from Fig. 5 that an additional distance of ~1 cm between hits is required in order to fully restore the coordinate reconstruction quality.

4. TRACK RECONSTRUCTION PROCEDURE

The track reconstruction method is based on the Kalman filtering technique (see, e.g. [17]). The efficiency of track reconstruction is plotted as a function

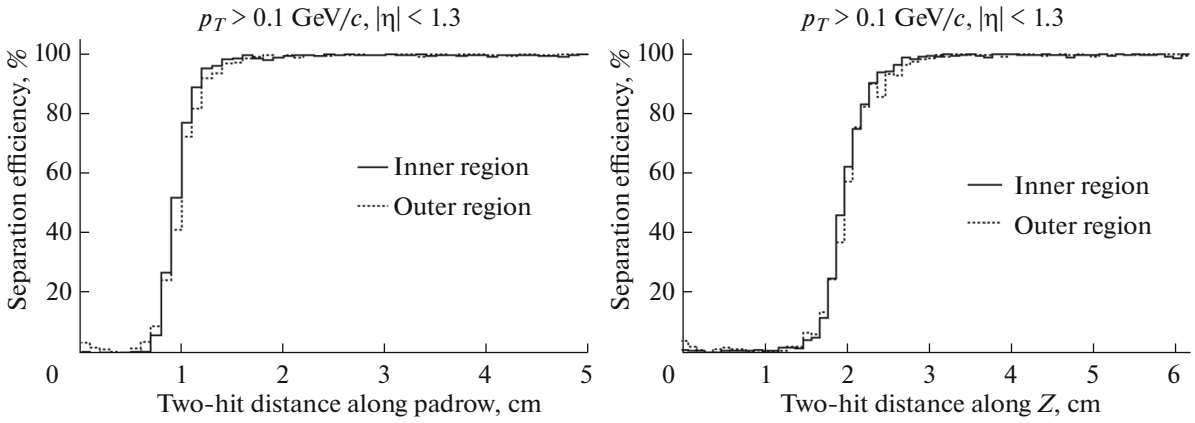

Fig. 4. Two-hit separation efficiency along the pad row direction (left) and along the drift direction (right). The distance in the orthogonal direction is below 0.1 cm. Considered are two-hit combinations from tracks with $|\eta| < 1.3$ and $p_T > 0.1$ GeV/c.

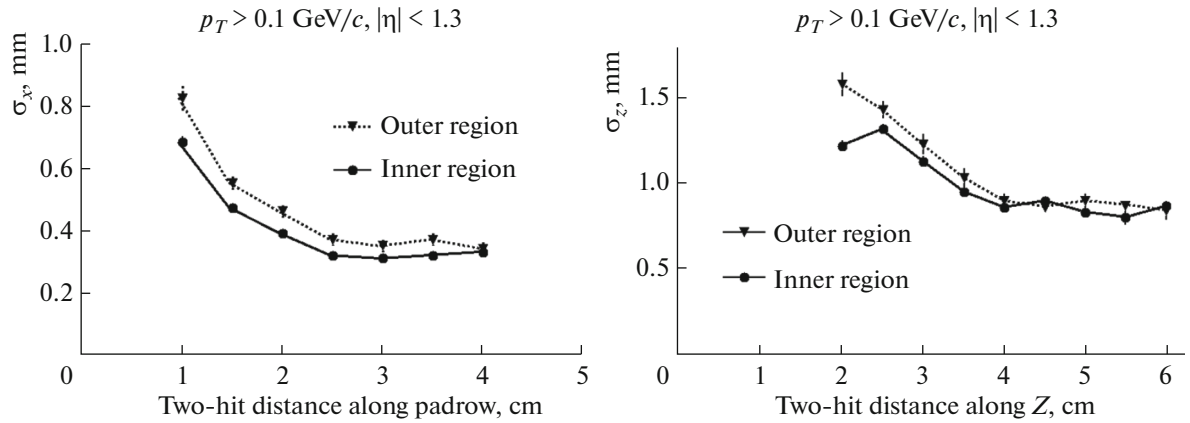

Fig. 5. Coordinate resolution along the pad row direction (left) and along the drift direction (right) as functions of the 2-hit separation for hit pairs as in Fig. 4.

of transverse momentum in Fig. 6 and as a function of pseudorapidity in Fig. 7. For the primaries, the TPC coverage and the number of space points allow us to reconstruct charged particle tracks up to $|\eta| = 1.7$ (efficiency above 90%). The secondary track sample on the plots contains particles produced within 50 cm of the primary vertex both in transverse and longitudinal directions, including electrons and positrons from the photon conversion. They are mostly responsible for the slow decrease of the tracking efficiency for p_T below 0.7 GeV/c in Fig. 6 and lower overall efficiency than for primary tracks in Fig. 7. This efficiency loss is due to the fact that a significant fraction of the conversion electrons is produced relatively far from the interaction point and the reconstruction procedure requires additional tuning to better handle them. In the realistic environment one should expect to reconstruct "clone" and "ghost" tracks. Track definition is the following: tracks having more than 50% of hits from the same particle are defined as "good". Otherwise they are considered as "ghosts". Two or more "good" tracks from the same particle (e.g., due to track splitting) are called "clones". As can be seen in Figs. 6 and 7, the fraction of clones is below 2% over the TPC pseudorapidity acceptance and for the entire p_T-spectrum, while the number of ghosts is very small and slightly grows with increasing occupancy at larger pseudorapidities.

In Fig. 8 the transverse momentum resolution of the MPD TPC (σ_{p_T}/p_T) is shown as a function of p_T (left panel) and η (right plot). The momentum resolution degrades rapidly above $\eta = 1.4$ due to decrease of the number of TPC space points, however the current MPD tracking performance in the large-η region can be improved in the future if several tracking chambers (based on GEM technology, for example) are installed between the beam pipe and the TPC inner cylinder (as was observed from some preliminary MPD studies).

Some other TPC performance results for primary particles are shown in Figs. 9 and 10. The left panel of

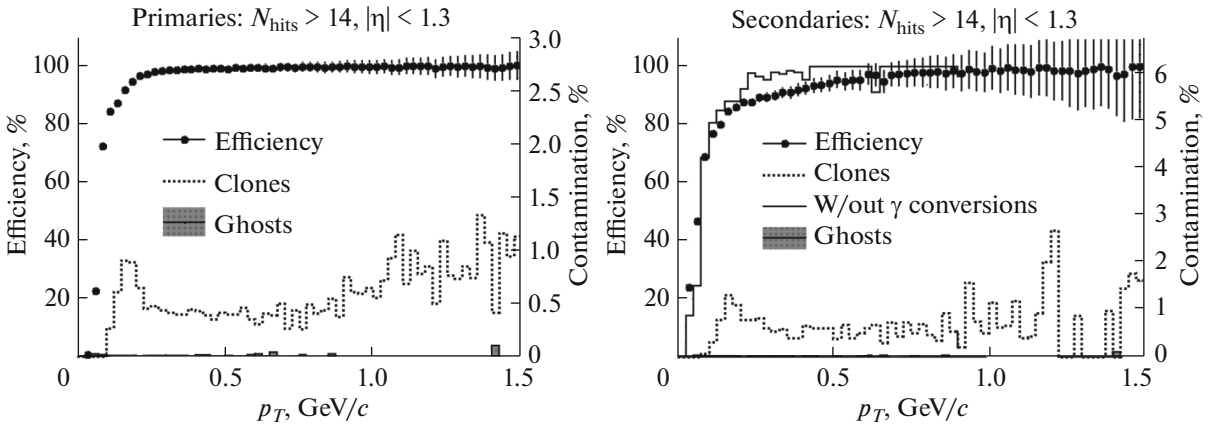

Fig. 6. Track reconstruction efficiency and contamination (percentage of clone and ghost tracks) as a function of track p_T for primary (left) and secondary (right) particles with $|\eta| < 1.3$. Left and right scales represent respectively the efficiency and contamination. Solid line on the right plot corresponds to the secondary track efficiency excluding electrons from the photon conversion.

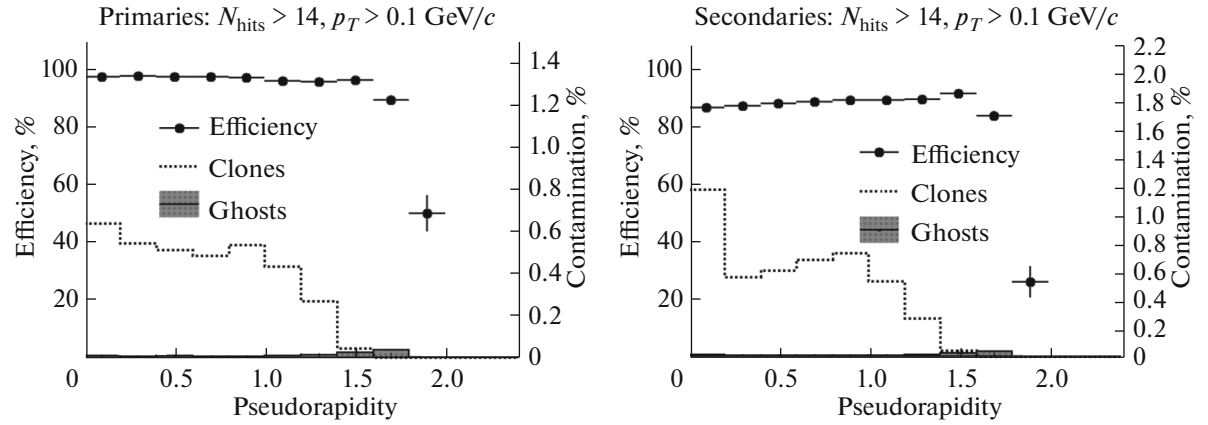

Fig. 7. Track reconstruction efficiency and clone and ghost contamination as functions of pseudorapidity for primary (left panel) and secondary (right panel) particles with momenta $p_T > 0.1$ GeV/c. The efficiency and contamination are labeled on the left and right vertical scales, respectively.

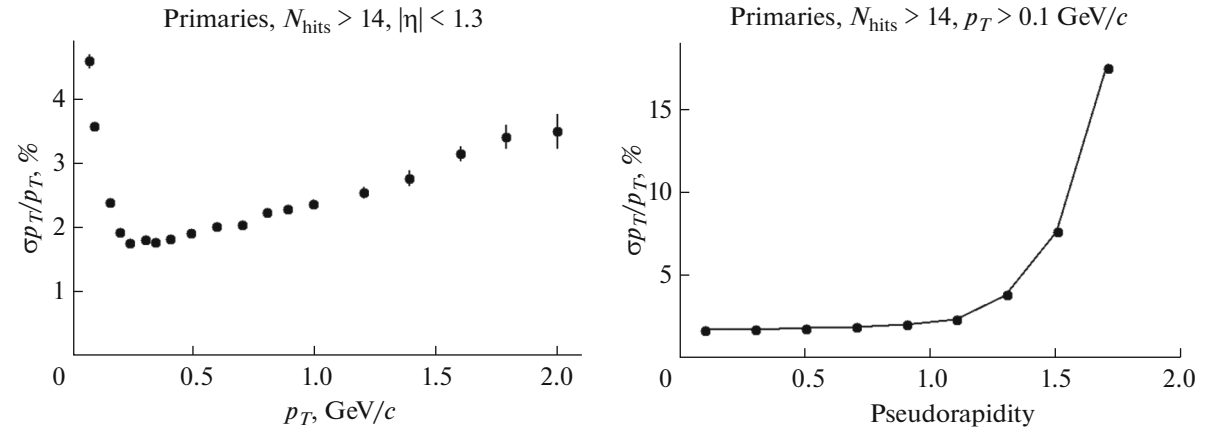

Fig. 8. Left—relative transverse momentum error versus p_T for primary tracks with $|\eta| < 1.3$; right—relative transverse momentum error versus pseudorapidity for primary tracks with momentum >0.1 GeV/c.

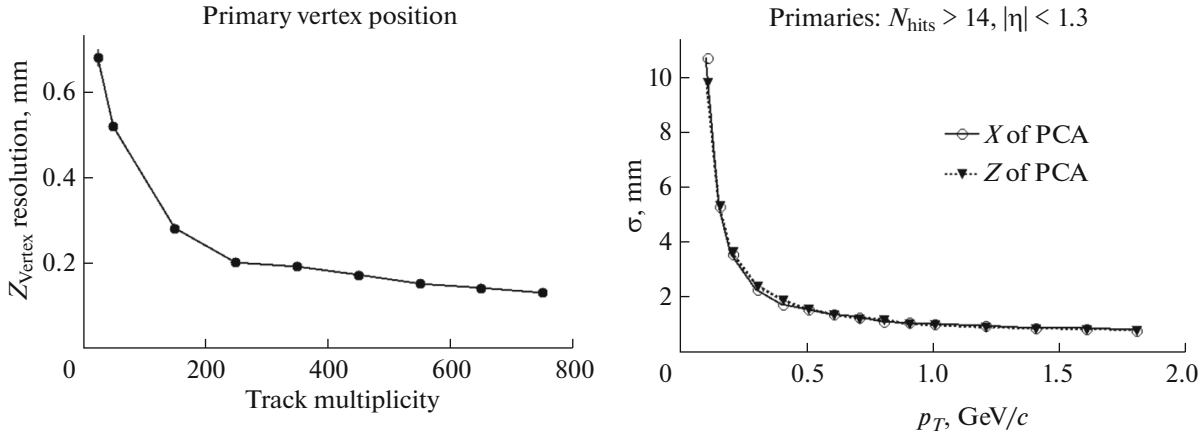

Fig. 9. Left—the longitudinal position error of the reconstructed primary vertex as a function of track multiplicity; right—transverse and longitudinal position errors at the point of the closest approach (PCA) to the interaction point for TPC reconstructed primary tracks within $|\eta| < 1.3$ versus particle transverse momentum.

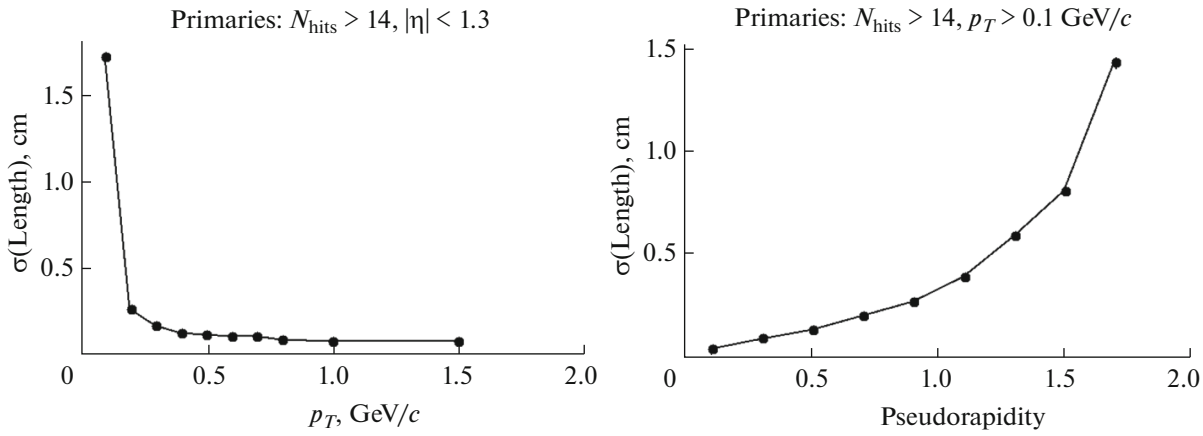

Fig. 10. Reconstructed primary track length uncertainty as a function of transverse momentum (left) and pseudorapidity (right).

Fig. 9 indicates the precision of the reconstructed interaction point (along the beam direction) as a function of the charged track multiplicity in the event. As can be seen, the accuracy of the primary vertex reconstruction varies from about 150 microns to approximately 700 μm in central and peripheral collisions, respectively. On the right panel of Fig. 9 the transverse and longitudinal position errors at the point of the closest approach (PCA) to the interaction vertex are plotted as functions of the track transverse momentum. Because of the relatively large distance between the interaction point and the first measured point inside the TPC (≈40 cm) extrapolation of low momenta tracks to the primary vertex is not very accurate. For the second stage of the project realization (after the year 2023), a silicon vertex detector will be added to the MPD setup providing space point measurements with a typical precision of tens of microns. Figure 10 shows the uncertainty in the determination of the track length as a function of p_t (left panel) and η (right plot).

The distribution of the TPC hit charges along a track follows the Landau one for ionizing particles. It has an asymmetric probability density function with a long upper tail [18]. The truncation procedure, i.e. dropping of 30% of the hits with the largest energy deposit, transforms the Landau distribution to a more Gaussian-like. In Fig. 11 (left panel) the truncated energy loss dE/dx for pions, kaons, and protons (from left to right) is plotted as a function of momentum. The achieved dE/dx resolution of 6–7% (see the right panel of Fig. 11) allows us to discriminate charged pions from kaons up to momenta of ~0.7 GeV/c and kaons from protons up to ~1.1 GeV/c.

5. TPC-TOF MATCHING

The MPD Time Of Flight (TOF) detector will be made of Multigap Resistive Plate Chambers (MRPCs) with a strip readout [19]. The detector provides both the time and coordinate measurements

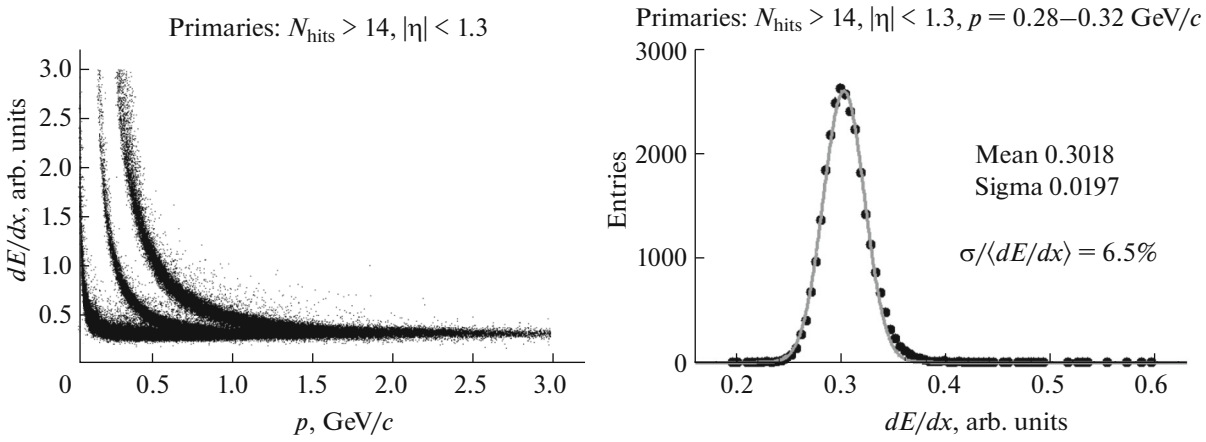

Fig. 11. Left—specific energy loss dE/dx as a function of momentum; right—energy loss distribution for pions with $p = 0.28–0.32$ GeV/c fitted to the Gaussian.

with accuracies of ~80 ps and ~0.5 cm, respectively. The TOF hit longitudinal coordinate (along the beam direction) is reconstructed as a position of the strip with the largest signal from a cluster of fired strips produced by a track, while the transverse coordinate (in $r-\varphi$ direction) is found from an arrival time difference of the signals from both ends of the strips.

The matching procedure of the reconstructed in the TPC tracks with hits in the TOF detector consists of the track extrapolation to the TOF surface and finding a nearest to the extrapolated point TOF hit within a pre-set window ("matching window"). The matching window size is taken as a compromise between the TOF intrinsic performance numbers (time and coordinate resolutions) and an overall TOF occupancy in heavy-ion collisions. In Fig. 12 the TOF (mis)matching efficiency is plotted as a function of the total momentum. As already mentioned, the results are obtained for central Au + Au collisions at $\sqrt{s_{NN}} = 9$ GeV and data points are averaged over the entire TOF acceptance of $|\eta| < 1.4$. The efficiency is defined as a fraction of tracks having produced a Monte Carlo point in the TOF and matched with any TOF hit according to the described procedure. If such a match is with a wrong hit, it is also considered as a mismatch. The overall efficiency is about 90% and it is dropping below 80% for track momenta below 250 MeV/c because of the multiple scattering which makes the difference between the expected positions of the extrapolated tracks and the actual ones larger than the size of the matching window in some cases. The errors in the extrapolation for low momentum tracks also cause the growing of the number of wrongly matched TPC track extrapolations and TOF hits (see triangles in Fig. 12 for mismatches), nevertheless, for momenta above 200 MeV/c (a typical low-momentum cutoff in the analysis) the fraction of the TPC-TOF mismatches is below 3%.

6. PARTICLE IDENTIFICATION

Particle identification (PID) in the MPD experiment can be achieved by using the information about the energy losses (dE/dx) in the TPC gas and the time-of-flight from the TOF detector. For optimal performance the PID procedure should rely on a good knowledge of the detector characteristics such as the momentum dependence of the average energy loss as well as the variation of the dE/dx and mass-squared resolutions for each particle specie. Based on this information a vector of probabilities to be a particle of a particular sort is assigned to each track and the highest probability defines the particle specie.

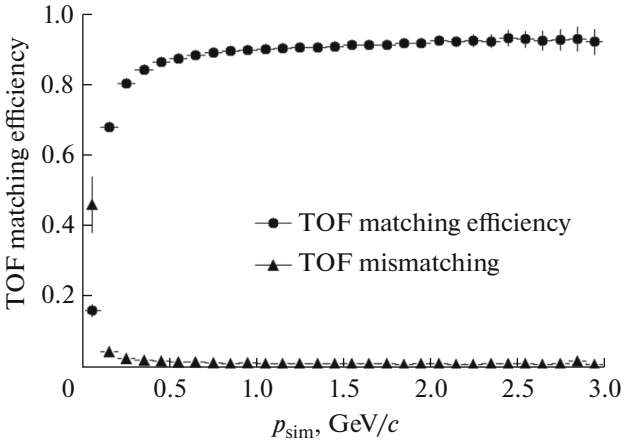

Fig. 12. TOF matching efficiency (circles) and fraction of mismatched tracks (triangles) in heavy-ion collisions as a function of the total momentum.

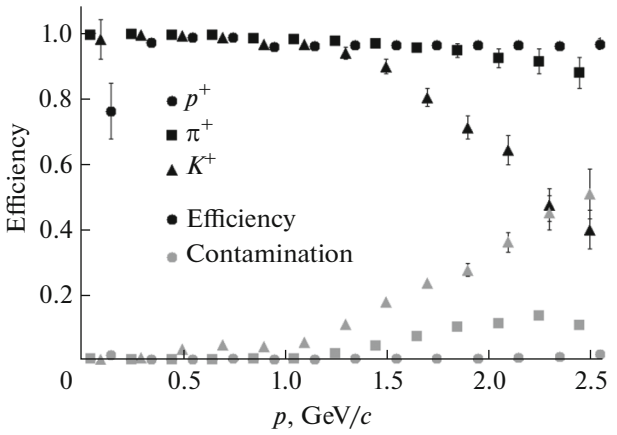

Fig. 13. Particle identification efficiency for positively charged hadrons (dark symbols) and a fraction of wrongly identified species (grey symbols) in Au + Au collisions at $\sqrt{s_{NN}}$ = 9 GeV.

The MPD performance for a discrimination of hadrons in minimum bias Au + Au collisions at $\sqrt{s_{NN}}$ = 9 GeV, produced by the DCM-QGSM event generator, is demonstrated in Fig. 13, where the fraction of the correctly identified particles is shown as a function of momentum (dark symbols). This fraction is above 90% for protons and positively charged pions up to p = 2.5 GeV/c, while the percentage of the cases with a wrong identification is below 10%. With the chosen set of cuts, charged kaons can be identified up to $p \sim 1.7$ GeV/c with an approximately 80% efficiency and 20% contamination at the PID limit. Making the selection criteria for kaons tighter, the achieved contamination level can be decreased further resulting in a lower value for the PID efficiency.

7. HYPERON RECONSTRUCTION

The approaches to the data simulation and reconstruction presented above and their software implementations were tested using Λ-hyperon reconstruction in minimum bias Au + Au collisions at $\sqrt{s_{NN}}$ = 9 GeV as a physics case. The primary and secondary vertices were reconstructed making use of similar methods based on the Kalman filtering formalism [20]. Figure 14 demonstrates that there are clear Λ-peaks in the invariant mass distributions of protons and negatively charged pions obtained with the current ("realistic") version of the particle identification and the perfect one (i.e. when proton and pion are known from the MC truth information). The analysis details can be found in [3, 5]. We only mention here that the invariant mass spectra are obtained using selection cuts corresponding to the maximum value of the peak significance $S/\sqrt{S+B}$, where S and B are total numbers of signal (described by the Gaussian) and background (polynomial function) combinations inside ±2σ interval around the peak position, and the efficiency values shown are with respect to all Λ-hyperons produced within 50 cm from the interaction point.

8. CONCLUSIONS AND PLANS

The "realistic" TPC response simulation for the MPD detector at NICA has been developed and implemented within the MpdRoot software package. The results, obtained with the updated simulation and reconstruction chain, demonstrate the adequate MPD tracking and PID performance within the pseudorapidity range of $|\eta| < 1.3$. The detector characteristics at $|\eta| > 1.3$, including those for strange hyperon reconstruction, can be further improved following the large-η detector introduction and additional tuning of the reconstruction algorithm.

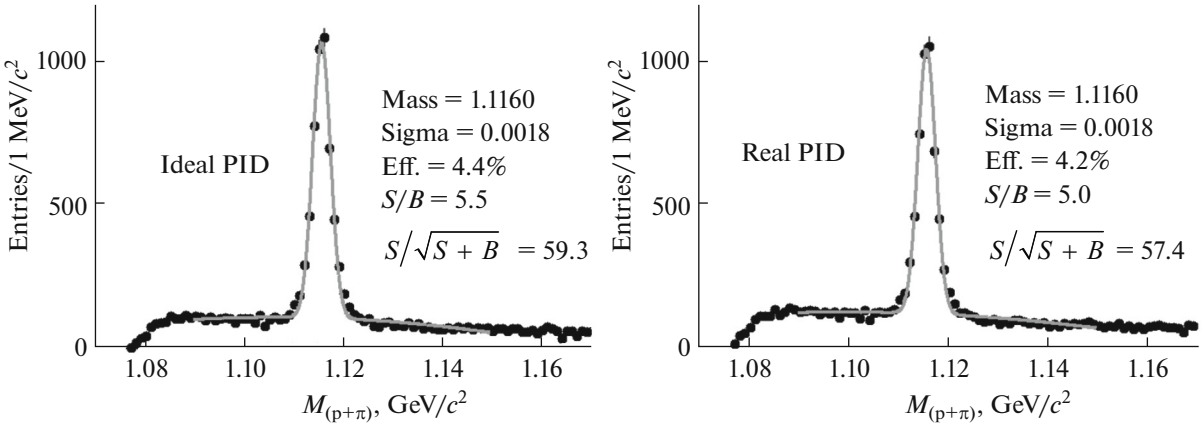

Fig. 14. Reconstructed invariant mass of proton and π^-. Left—perfect charged particle identification; right—"realistic" particle identification.

9. ACKNOWLEDGMENTS

Authors would like to thank S. Merts and P. Batyuk for their work on earlier versions of the TPC digitization software package and S. Lobastov for the implementation of the TPC-TOF matching procedure. The investigation has been performed at the Laboratory of High Energy Physics, JINR.

REFERENCES

1. V. D. Kekelidze, R. Lednicky, V. A. Matveev, I. N. Meshkov, A. S. Sorin, and G. V. Trubnikov, "Three stages of the NICA accelerator complex," Eur. Phys. J. A **52**, 211 (2016).
2. V. Golovatyuk, V. Kekelidze, V. Kolesnikov, O. Rogachevsky, and A. Sorin, "The multi-purpose detector (MPD) of the collider experiment," Eur. Phys. J. A **52**, 212 (2016).
3. M. Ilieva, V. Kolesnikov, Yu. Murin, D. Suvarieva, V. Vasendina, A. Zinchenko, E. Litvinenko, and K. Gudima, "Evaluation of the MPD detector capabilities for the study of the strangeness production at the NICA collider," Phys. Part. Nucl. Lett. **12**, 100 (2015).
4. V. Vasendina, V. Jejer, V. Kolesnikov, S. Lobastov, G. Musulmanbekov, I. Tyapkin, and A. Zinchenko, "Study of the MPD detector capabilities for electron-positron pair measurements at the NICA collider," Phys. Part. Nucl. Lett. **10**, 769 (2013).
5. M. Ilieva, V. Kolesnikov, D. Suvarieva, V. Vasendina, and A. Zinchenko, "Reconstruction of multistrange hyperons with the MPD detector at the NICA collider: a Monte Carlo feasibility study," Phys. Part. Nucl. Lett. **12**, 618 (2015).
6. http://urqmd.org/.
7. V. D. Toneev and K. K. Gudima, "Particle emission in light and heavy ion reactions," Nucl. Phys. A **400**, 173 (1983).
8. N. S. Amelin, K. K. Gudima, and V. D. Toneev, "Ultrarelativistic nucleus-nucleus collisions within a dynamical model of independent quark-gluon strings," Sov. J. Nucl. Phys. **51**, 1093 (1990).
9. N. S. Amelin, L. V. Bravina, L. P. Csernai, V. D. Toneev, K. K. Gudima, and S. Y. Sivoklokov, "Strangeness production in proton and heavy ion collisions at 200-A-GeV," Phys. Rev. C **47**, 2299 (1993).
10. L. A. Shepp and Y. Vardi, "Maximum likelihood reconstruction for emission tomography," IEEE Trans. Med. Imaging **1**, 113 (1982).
11. L. B. Lucy, "An iterative technique for the rectification of observed distributions," Astron. J. **79**, 745 (1974).
12. W. H. Richardson, "Bayesian-based iterative method of image restoration," J. Opt. Soc. Am. **62**, 55 (1972).
13. G. D. Agostini, "A multidimensional unfolding method based on Bayes' theorem," Nucl. Instrum. Methods Phys. Res., Sect. A **362**, 487 (1995).
14. E. A. Kolganova, G. A. Ososkov, and E. L. Kosarev, "Superresolution algorithms for data analysis of discrete detectors in nuclear physics," Nucl. Instrum. Methods Phys. Res., Sect. A **443**, 464 (2000).
15. A. Zinchenko et al. (ALICE Collab.), "A new approach to cluster finding and hit reconstruction in cathode pad chambers and its development for the forward muon spectrometer of ALICE," Nucl. Instrum. Methods Phys. Res., Sect. A **502**, 778 (2003).
16. M. Anderson et al. (STAR Collab.), "The star time projection chamber: a unique tool for studying high multiplicity events at RHIC," Nucl. Instrum. Methods Phys. Res., Sect. A **499**, 659 (2003).
17. R. Fruhwirth, "Application of Kalman filtering to track and vertex fitting," Nucl. Instrum. Methods Phys. Res. **262**, 444 (1987).
18. L. Landau, "On the energy loss of fast particles by ionization," J. Phys. USSR **8**, 201 (1944).
19. MPD TOF Technical Design Report. http://mpd.jinr.ru/wp-content/uploads/2017/07/TDR_TOF_MPD_v2_20-17_07_2017.pdf.
20. R. Luchsinger and Ch. Grab, "Vertex reconstruction by means of the method of Kalman filter," Comput. Phys. Commun. **76**, 263 (1993).